

Performance of single-photons communication using the multi-channel frequency coding scheme

JIANYONG HU, MINGYONG JING, GUOFENG ZHANG, CHENGBING QIN, LIANTUAN XIAO,* AND SUOTANG JIA

¹State Key Laboratory of Quantum Optics and Quantum Optics Devices, Institute of Laser Spectroscopy, Shanxi University, Taiyuan 030006, China

²Collaborative Innovation Center of Extreme Optics, Shanxi University, Taiyuan 030006, China
xlt@sxu.edu.cn

Abstract: In this paper, optical communication at the single-photon level is experimentally demonstrated by using a multi-channel frequency coding scheme in which the information is decoded by using the single-photons modulation spectrum. By using the modulation spectrum, the coding scheme could work normally in a channel with high loss and noise. Besides, multiple modulation frequency components could be used in a wide bandwidth regardless of frequency aliasing; therefore, the multi-channel frequency coding scheme makes it possible for high-capacity single-photons communication.

© 2018 Optical Society of America under the terms of the [OSA Open Access Publishing Agreement](#)

1. Introduction

Long-distance optical communication, such as the satellite-to-ground communication and the interplanetary Internet, has gained considerable attention in recent years. However, in these cases, channel noise and loss caused by atmospheric turbulence and irradiance fluctuation seriously affect the transmission capacity [1–5]. Despite narrow beam divergence and high energy density of laser, in some cases, the received signal is still at the single-photon level [6].

The optical homodyne phase-shift-keying modulation and the pulse-position modulation (PPM) are coding schemes that are commonly used in the field of power-limited communication [7–9]. In these schemes, photon counting is used to separate the signal from background noise, which is vulnerable to the noise photons and dark counts [10–17].

Quantum statistical properties of radiation can be obtained once enough photons are collected regardless of channel loss and noise. Time domain quantum statistical properties are usually characterized by the second-order correlation or the Mandel- Q parameter [18–20]. The second-order correlation is robust in judging whether an optical field is a single photon source, while the time-dependent Mandel- Q parameter can reflect the statistical properties over a large time-scale [21]. However, they fail to transmit information efficiently. Recently, the single-photons modulation spectrum (SPMS) has been introduced to investigate the statistical properties of radiation sources in the frequency domain [22, 23]. It is shown that modulated frequency components can be extracted directly from the SPMS within a short integration time.

In this paper, a multi-channel frequency coding (MCFC) scheme is proposed and experimentally demonstrated, which shows the possibility for high-capacity single-photons communication. The factors that affect the error rate of MCFC are investigated. The formula for transmission capacity when considering the error rate is also given.

2. The principle of the MCFC scheme

Photon counting of weak coherent state $|\alpha\rangle$ at the single-photon level obeys the Poisson distribution p_n which means the photon arrival time is totally random. After the detection, the Discrete Fourier Transform (DFT) of the output of the single-photon detector (SPD) shows as

white noise spectrum [23, 24]. However, if a coherent state is modulated by an intensity modulator with a sinusoidal function, the probability of detecting a photon becomes $|\alpha|^2(\sin(2\pi f_M t + \theta) + 1)/2$, where f_M is the modulation frequency, and θ is the initial phase of the sinusoidal function [25–27]. The characteristics of the modulated weak coherent state can be revealed by the second-order correlation function or the Mandel- Q parameter (see Appendix A); however, the modulation frequency cannot be read directly from them. Instead of the white noise spectrum, the spectrum of the modulated weak coherent state is a superposition of the white noise and the characteristic spectral line located at f_M . The modulation frequency can be directly derived from the SPMS by locating the position of the characteristic spectral line [28].

In addition, according to the non-uniform sampling theory, the frequency estimation could be performed in a wide range without frequency aliasing even if the sampling rate is much smaller than the Nyquist rate which is twice the bandwidth of the signal [29–32]. In our experiment, the Poisson distribution is an intrinsic property of the weak coherent state, and in principle, the detection time of each photon is totally random. Therefore, the modulation frequency can be decoded in a wide frequency bandwidth without frequency aliasing.

After the modulation at the transmitting terminal, suppose that the receiver detected N photons within an integration time T_i , and the arrival time of each photon is $\tau_1, \tau_2, \dots, \tau_i, \dots, \tau_N$ ($0 < \tau_i \leq T_i$). The DFT of the detected photon sequence can be expressed as

$$X(f) = \sum_{i=1}^N A_i e^{-j2\pi f \tau_i} \quad (1)$$

where $A_i = 1$ is the amplitude of the output pulse of the SPD. The probability density distribution is transformed into $P_{(t)} = (1 + \sin(2\pi f_M t + \theta))/2$, without loss of generality, we assume $\theta = 0$. The expectation of the Fourier transform of the modulated photon sequence is

$$\begin{aligned} X_{(\omega)} &= \int_0^{T_i} A \cdot e^{-j\omega t} \cdot (\sin(2\pi f_M t) + 1) \cdot dt \\ &= -\frac{j(1 - e^{j\omega T_i})}{\omega} + \frac{e^{-j\omega T_i} \cdot (-2\pi f_M e^{j\omega T_i} + 2\pi f_M \cdot \cos(2\pi f_M T_i) + j\omega \cdot \sin(2\pi f_M T_i))}{\omega^2 - 4f_M^2 \pi^2}, \end{aligned} \quad (2)$$

where A is the normalization coefficient. The first item to the right of Eq. (2) is a direct current item, which shows as a low-frequency noise. The second item is an alternating current item, which carries the information of the modulation frequency. Equation (2) indicates that the modulation frequency can be read out directly from the SPMS once sufficient modulated photons are detected.

In the MCFC scheme, by encoding the modulation frequencies at the transmitting terminal and decoding the modulation frequencies at the receiving terminal, the information can be transmitted. The SPMS can be used to extract frequency information in a wide bandwidth and won't be disturbed by high order frequency components of modulation frequency [29], which would significantly increase the available degrees of freedom for encoding, and hence increases the transmission capacity.

3. Experimental setup and results

3.1 Experimental setup

To demonstrate the MCFC scheme, a typical color image was transmitted, as shown in Fig. 1. Each pixel of the image was described using three parameters: R, G, and B (red, green and blue), which denote the gray values of the three primary colors. In the experiment, the original color image was first decomposed into three monochromatic images: red, green and blue, at the transmitting terminal. To transmit the image, first, the relationship between the modulation frequencies and the gray values was built up, as noted in Table 1. The modulation

frequency band was divided into three sub-bands: 60~80 kHz, 40~60 kHz, and 20~40 kHz which correspond to the gray values of red, green and blue respectively. The gray values of each primary color were divided into eleven (0~10) levels, and the channel spacing between the adjacent frequency channels was set at 1.0 kHz. Here we chose eleven levels as an example, if one wants to improve the quality of the image, more levels could be used, for example, 256 levels. Then three modulation signals with different frequencies were applied to the optical intensity modulator (EOSPACE). Each frequency represented the gray value of one primary color. An optical attenuator was used to simulate the channel loss. At the receiving terminal, the SPD (QCD-300, quantum efficiency 10%) was used to detect these modulated photons. The arrival time τ_i ($0 < \tau_i < T_i$) of each photon is recorded by a time interval analyzer (GT658, resolution 75 ps). By implementing the DFT on the arrival time of the photons, the modulation frequencies were decoded.

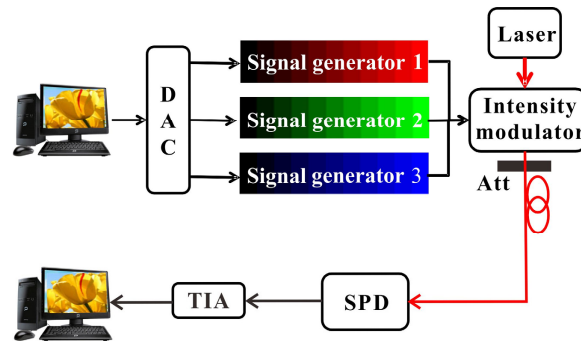


Fig. 1. Experimental setup of the MCFC scheme. DAC: Data acquisition card (NI 6259); Att: Optical attenuator; SPD: Single-photon detector. TIA: Time interval analyzer.

Table 1. The corresponding relationship between the gray values of the images and the modulation frequencies.

Red level											
f_M (kHz)	75	74	73	72	71	70	69	68	67	66	65
Green level											
f_M (kHz)	55	54	53	52	51	50	49	48	47	46	45
Blue level											
f_M (kHz)	35	34	33	32	31	30	29	28	27	26	25

3.2 Experimental results

Figure 2 presents one of the spectrums of the detected photons within one integration time T_1 . It shows that the frequencies of the modulation signal used at the transmitting terminal are 25 kHz, 50 kHz, and 71 kHz respectively. The spectrum in Fig. 2 is a superposition of the characteristic spectral lines and the white noise floor which is mainly caused by shot noise, as we mentioned in section 2. According to the preset relationship between the modulation frequencies and the gray values shown in Table 1, these characteristic spectral lines represent the blue 10th level, green 5th level and red 4th level, respectively. By using the information that we got from this spectrum, one pixel in the image was recovered. The whole image can be recovered after the information for all pixels is received. In Fig. 3, the whole image is shown, a_1 - a_4 are the original images, and b_1 - b_4 and c_1 - c_4 are the transmitted images when the mean signal photon count is 80 kcps (kilo counts per second) and 10 kcps, respectively. The integration time T_1 is 1 ms, and system repetition frequency (i.e. the trigger frequency of gated SPD) is 10 MHz. The images b_1 - b_4 in Fig. 3 are recovered without errors, but the images c_1 - c_4 have errors (image defects) due to the low mean signal photon count. The relationship between the error rate and the mean signal photon count is given in the discussion section.

The MCFC scheme can be used to transmit text, images, video, and other file formats; the corresponding relationship between the files and the modulation frequencies would just need to be built up. For example, Table 2 shows a relationship between Roman characters and the modulation frequencies. Furthermore, the total available modulation bandwidth could be divided into a range of sub-bands which could be allocated to different users or different information types.

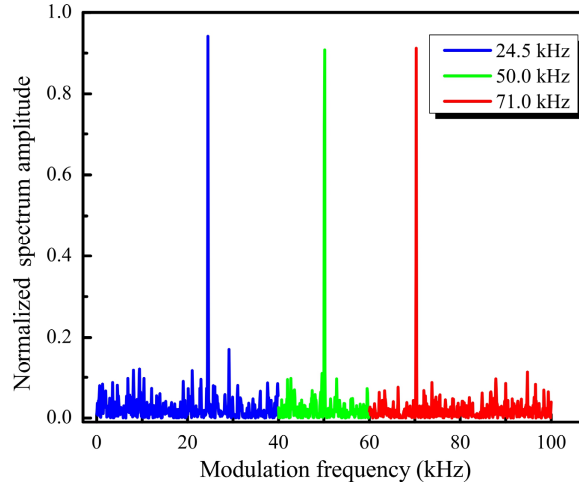


Fig. 2. The spectrum of the detected photon sequence. The mean signal photon count is 80 kcps, the system repetition frequency is 10 MHz, and the integration time is 1 ms.

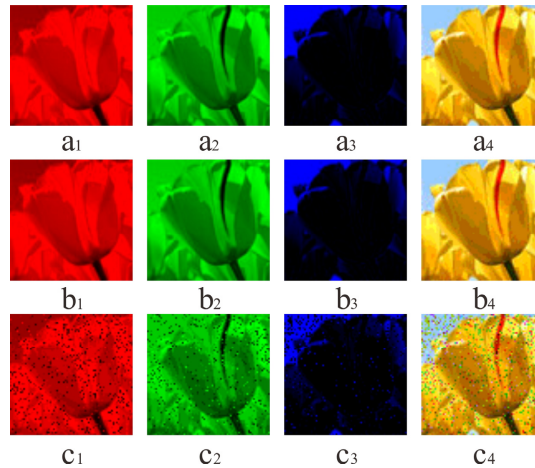


Fig. 3. Image transmission with the MCFC scheme. a_1 , a_2 and a_3 are the three monochromatic images decomposed from original image a_4 . b_1 , b_2 , and b_3 are the received monochromatic images when the mean signal photon count is 80 kcps. b_4 is the recovered color image produced by composing b_1 , b_2 , and b_3 . c_1 , c_2 , c_3 , and c_4 are the equivalent received images when the mean signal photon count is 10 kcps.

Table 2. The corresponding relationship between Roman characters and modulation frequencies.

Character	A	B	C	D	E	F	G	H	I
Frequency (kHz)	50	51	52	53	54	55	56	57	58
Character	J	K	L	M	N	O	P	Q	R
Frequency (kHz)	59	60	61	62	63	64	65	66	67
Character	S	T	U	V	W	X	Y	Z	
Frequency (kHz)	68	69	70	71	72	73	74	75	

4. Discussion

For an MCFC communication system with a fixed channel spacing f_s , the transmission capacity is determined by the total available modulation bandwidth. Evidently, for a given system there is always a finite optimal number of frequency channels M_{opt} [29]. If frequency channel $M < M_{\text{opt}}$, it is a waste of spectrum resource. In contrast, if $M > M_{\text{opt}}$, the disturbance between adjacent channels would occur. The optimal number of frequency channels, that is, the degrees of freedom that can be used for encoding, would be

$$M_{\text{opt}} = \frac{B}{f_s} + 1, \quad (3)$$

where B is the total available modulation frequency band and f_s is the channel spacing which is determined by time jitter and integration time, respectively. If there are k ($k \geq 1$) frequency components contained in the modulation signal, the number of effective frequency channels would be the number of combinations of k available frequencies

$$M_{\text{max}} = \frac{M_{\text{opt}}!}{k!(M_{\text{opt}} - k)!}, \quad (4)$$

when one chose $k = 1$, $M_{\text{opt}} = M_{\text{max}}$. The number of frequency channels is the degree of freedom that can be used for encoding the information. The transmission capacity can be expressed as

$$I = \frac{1}{T_I} \text{Log}_2 M_{\text{max}}. \quad (5)$$

In our experiment, limited by the repetition frequency of our gated SPD, the maximal modulation frequency realized in the experiment is 4 MHz. The channel spacing used in the experiment is $f_s = 1.0$ kHz and integration time $T_I = 1$ ms, while the frequency component k is 1 or 3, the transmission capacity is 11.9 kbps or 33.3 kbps, respectively.

The transmission capacity analyzed above didn't take the error rate into consideration. According to Shannon's noisy channel coding theorem, the maximal transmission capacity is limited by the error rate. In our experiment, the error rate is mainly dependent on the channel loss, noise, channel spacing, frequency components and integration time. Quantitative analysis of the error rate is performed through numerical simulation, as shown in Fig. 4 and Fig. 5. The algorithm used for the simulation is given in Appendix B.

Quantum shot noise is an intrinsic property of the weak coherent state, which would result in the fluctuation of the characteristic spectral lines. The distribution of the amplitude of the characteristic spectral lines can be characterized by their mean value $E[A_S]$ and variance σ_S . Shot noise, background light and dark counts of the SPD result in an increase of noise floor. The distribution of the amplitude of the noise floor can also be characterized by its mean value $E[A_B]$ and variance σ_B . When the amplitude of the characteristic spectral line A_S is bigger than the noise floor A_B , the information can be decoded correctly. For the red line A shown in Fig. 4, the gray dashed line D is the boundary of the noise floor. Both the signal photon count and the noise photon count obey the Poisson distribution, the mean signal photon count and mean noise photon count is $N_{\text{signal}} = 80$ kcps and $N_{\text{noise}} = 0$ kcps, respectively. The noise peak of the red line is caused by the shot noise. The noise photon counts increase the noise floor, which may lead to the overlap of the amplitude distribution of the characteristic spectral line and the noise floor. Here, we consider a situation where the mean noise photon count is equal to the mean signal photon count, which is represented by the black dotted line in Fig. 4. Both the mean signal photon count and the mean noise photon count are 80 kcps. The black solid line B is the sum of the two black dotted lines; the boundary (the gray dashed line E) of the noise floor can be easily identified from it. With the

increase of the photon counts, the mean amplitude of the characteristic spectral line $E[A_S]$ increases faster than that of the noise floor. When the mean signal and mean noise photon counts are 160 kcps, the noise floor and characteristic spectral line distribution are split totally, as the blue line *C* shows in Fig. 4, the gray dashed line *F* is the boundary of the noise floor.

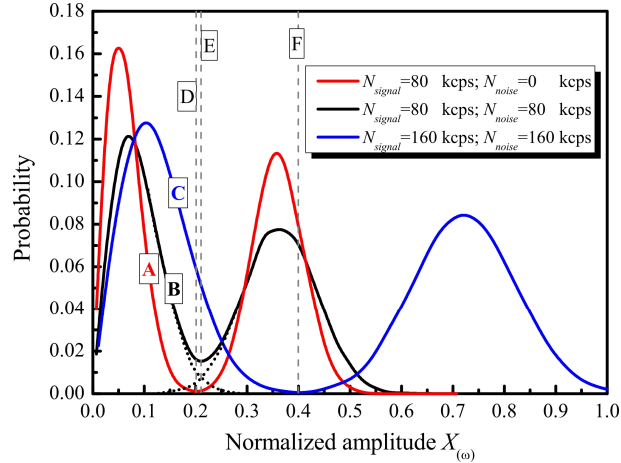


Fig. 4. (Simulation) The spectrum amplitude distribution of the characteristic spectral line and the noise floor. The mean signal photon count of red line *A*, black line *B*, and blue line *C* are 80 kcps, 80 kcps, and 160 kcps, respectively, while the mean noise photon counts are 0 kcps, 80 kcps, and 160 kcps, and the boundaries of noise floor are marked with gray dashed lines *D*, *E*, and *F*, respectively. The modulation frequency is 200 kHz.

The error rate is determined by the amplitude distribution of the characteristic spectral line and the noise floor. The amplitude of the characteristic spectral line and the noise floor obeys the Gaussian distribution. Once the noise amplitude is higher than the amplitude of the characteristic spectral line, the error code will be produced. Therefore, the error rate for a single frequency channel is

$$e_s = \int_0^\infty \frac{1}{\sqrt{2\pi}\sigma_S} e^{-\frac{(A_S - E[A_S])^2}{2\sigma_S^2}} \left(\int_{A_S}^\infty \frac{1}{\sqrt{2\pi}\sigma_B} e^{-\frac{(A_B - E[A_B])^2}{2\sigma_B^2}} dA_B \right) dA_S, \quad (6)$$

where A_S and A_B are the amplitudes of the characteristic spectral line and the noise floor; σ_S and σ_B are the variances of the characteristic spectral line and the noise floor. When there are M frequency channels, the error rate is $e = 1 - (1 - e_s)^M$. The error rate e increases with the number of frequency channels.

The noise count spreads its energy over a much wider range in the frequency domain. However, the modulated photon sequence has a definite frequency. Therefore, even with high noise count, it just slightly increases the noise floor in the frequency domain. Figure 5(a) shows the quantitative error rate of the MCFC scheme in a noisy environment. It shows that the error rate maintains a low level, even when the mean noise photon count is comparable with the mean signal photon count. As the blue line shows, the error rate is less than 10^{-6} when the signal photon count and noise photon count are both 160 kcps. When the mean noise photon count is zero, the error rate is only limited by the quantum shot noise.

Besides the noise count dependence, the error rate also correlates with the integration time T_I . As shown in Fig. 5(b), the error rate oscillates with integration time. In addition, the amplitude of the oscillation fades with the increase of the integration time and tends to be a certain level 10^{-5} . Further improvement of the error rate is limited by the quantum shot noise. In practical applications, the integration time should be as short as possible to obtain a higher

transmission capacity, as described in Eq. (5). The higher the modulation frequency, the shorter the integration time required. Therefore, only the lowest modulation frequency used in the system needs to be considered when determining the integration time. Figure 5(b) shows when the minimum modulation frequency is 10 MHz, 1 MHz, 100 kHz, 10 kHz and 1 kHz the integration time should be set at least 1 μ s, 10 μ s, 100 μ s, 1 ms and 10 ms, respectively.

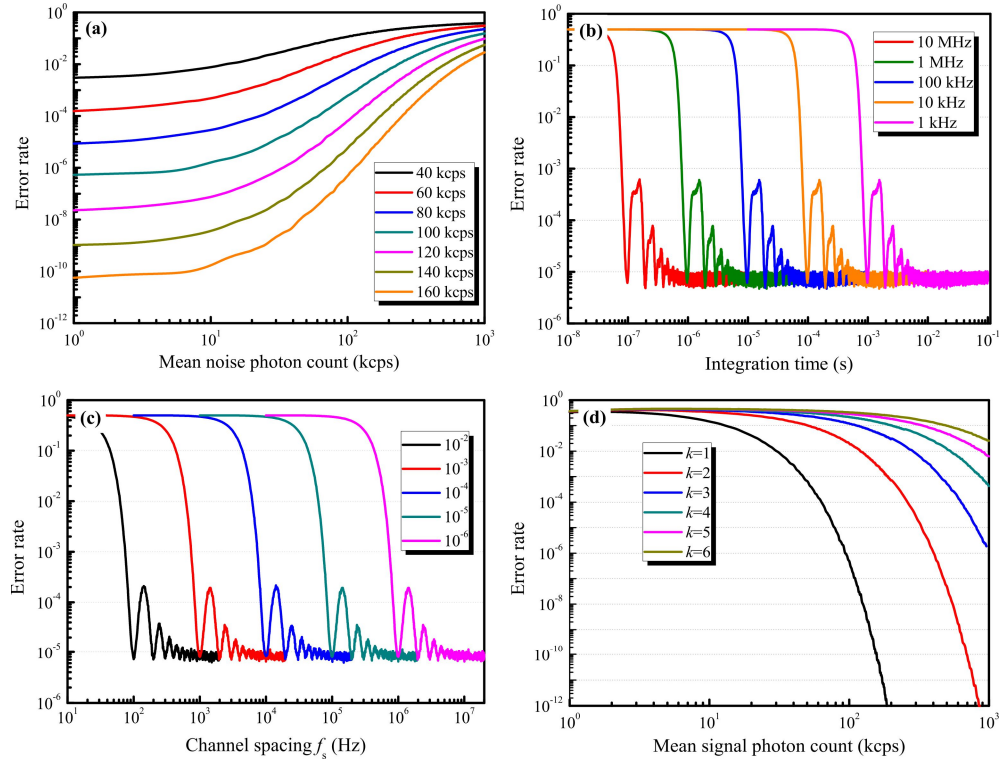


Fig. 5. (Simulation) (a) The impact of mean noise photon count on the error rate for different mean signal photon count. (b) The impact of integration time on the error rate. The error rate is oscillating as integration time increases and the period is $1/f_m$. The oscillation waveform correlates with the initial phase θ of the modulation signal. In this simulation, initial phase $\theta = 0$ and the mean signal photon count in each integration time was 80. (c) The impact of channel spacing on the error rate for different integration times. In (a), (b) and (c) only one frequency component is considered. In (d), the impact of mean signal photon count on error rate with different frequency components is shown. Here, k ($k = 1, 2, 3, 4, 5, 6$) is the number of frequency components.

The full width at half maximum of the characteristic spectral line is mainly influenced by the integration time. Channel spacing should be set properly to avoid the disturbance of adjacent frequency channels. Figure 5(c) shows the relationship between the error rate and the channel spacing for different integration times. The error rate decreases with a damped oscillation behavior when the channel spacing increases. To optimize the transmission capacity, small channel spacing is preferred. Therefore, the first trough of each line is the best channel spacing choice, as indicated by the red line, where the integration time is 1 ms and the channel spacing is set at 1 kHz.

The number of frequency components k also has its effect on the error rate, as shown in Fig. 5(d). The error rate increases obviously when there are more frequency components contained in the modulation signal. More photon counts are needed to keep the low error rate. For example, when the error rate is set at 10^{-5} , the detected mean signal photon count needs to be 80 kpcps for one frequency component and 720 kpcps for three frequency components. This characteristic results from the fact that the modulation signal is becoming more sophisticated

with the increase of the frequency components, and more photons are needed to recover the modulation frequency information.

The requirements of the error rate are different in various situations, but generally, 10^{-5} is enough for information transmission [7]. Figure 5 can be used as a reference for parameter selection for different error rate requirements. When considering the error rate, the transmission capacity is

$$I = \frac{1}{T_I} \text{Log}_2 M_{\max} (1 - H(p_e)), \quad (7)$$

where $p_e = M_{\max} e / 2(M_{\max} - 1)$ is the bit error rate, and $H(p_e)$ is the Shannon entropy. The derivation of Eq. (7) is given in Appendix C.

According to Eq. (7) and Eq. (4), the transmission capacity is mainly determined by the modulation frequency band B and the integration time T_I . If a free running detector is used, the modulation frequency band B and the integration time T_I are limited by the time jitter and the maximum count rate of the SPD, respectively. Therefore, with a more advanced SPD, the transmission capacity could be improved significantly. As shown in Fig. 6(a), the error rate increases with the modulation frequency when the time jitter is taken into consideration. When the error rate of 10^{-5} is required, the maximum modulation frequencies are 0.1 GHz and 1 GHz, while the time jitters are 400 ps and 45 ps, respectively. In this simulation, we assume that the time jitter obeys the Gaussian distribution and set the standard deviations equal to the mean values. For a certain error rate, the higher the count rate is, the shorter the integration time required will be, and according to Eq. (7), higher transmission capacity could be achieved. As shown in Fig. 6(b), when the count rate reaches to 100 MHz the transmission capacity reaches 7.9 Mbps with a 0.1 GHz modulation frequency band and 12.1 Mbps with a 1.0 GHz modulation frequency band.

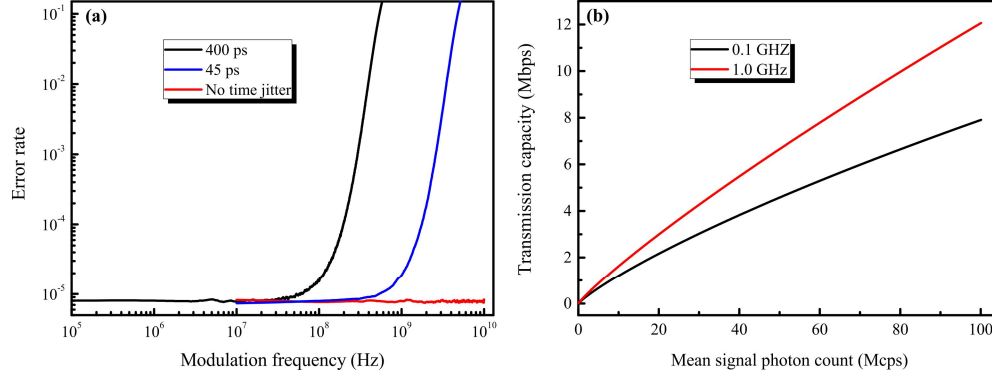


Fig. 6. (Simulation). (a) The error rate changes with the modulation frequency when the time jitter of an SPD is taken into consideration, here we assume a free running SPD is used. (b) Transmission capacity vs photon count rate. If the count rate is 100 MHz, the transmission capacity reaches 7.9 Mbps and 12.1 Mbps when the modulation frequency bands are 0.1 GHz and 1 GHz, respectively.

5. Conclusion

In this paper, the MCFC scheme has been proposed based on the properties of the SPMS, which are favorable to single-photons communication. In this scheme, the frequency information in a wide bandwidth could be obtained regardless of frequency aliasing, which significantly increased the degree of freedom that could be used for encoding, and hence enhanced the transmission capacity of the communication system. The frequency domain quantum statistical properties of the modulated optical field have been characterized by the SPMS.

A typical color image was transmitted to verify its feasibility. The error rate of the MCFC scheme, including its dependence on the mean noise photon count, the integration time, the channel spacing, and the number of frequency components has been investigated, which can help us to optimize the parameters of the communication system. Finally, the transmission capacity is presented when considering the error rate. The MCFC scheme could be used in quantum communications or long-distance free-space optical communications, such as the construction of interplanetary Internet.

Appendix A: second-order correlation function and Mandel-Q parameter

After the modulation, the distribution changing of coherent state can be characterized by the second-order correlation function and the Mandel- Q parameter, as shown in Fig. 7. The intensity (i.e. the probability that detect a photon) of modulated coherent state can be expressed as

$$I = \frac{|\alpha|^2}{2} [\sin(2\pi f_M t + \theta) + 1], \quad (8)$$

where $|\alpha|$ is the mean photon number, θ is the initial phase of the modulation signal. The probability of coincidence count in the measurement of the second-order correlation is

$$P = A \cdot \int_0^{T_I} (\sin(2\pi f_M t + \theta) + 1)(\sin(2\pi f_M (t + \Delta t + \theta) + 1)) dt, \quad (9)$$

where A is the normalization coefficient, T_I is the integration time, and Δt is the relative time delay. The measurement of the second-order correlation is shown in Fig. 7(a), the theoretical fitting is done by using Eq. (9). The modulation frequency we used is 200 kHz.

For a coherent state without modulation, the formula for calculating the Mandel- Q parameter is

$$Q = \frac{\langle n^2 \rangle - \langle n \rangle^2}{\langle n \rangle} - 1, \quad (10)$$

where

$$\langle n^2 \rangle = \sum_{n=0}^{\infty} \frac{(|\alpha|^2 T_I)^n e^{-|\alpha|^2 T_I}}{n!} n^2, \quad (11)$$

$$\langle n \rangle = |\alpha|^2 T_I. \quad (12)$$

T_I denotes the integration time, and $|\alpha|^2 T_I$ is the mean photon number per integration time. By substituting Eq. (11) and Eq. (12) into Eq. (10), we get $Q = 0$ which is not correlated with the integration time.

For the modulated coherent state, the probability of detecting n photons within the j th integration time T_I becomes a function of time.

$$p_n^M = \frac{\left[\int_{jT_I}^{(j+1)T_I} \frac{|\alpha|^2}{2T_I} (\sin(2\pi ft + \theta) + 1) dt \right]^n \cdot \exp \left[- \int_{jT_I}^{(j+1)T_I} \frac{|\alpha|^2}{2T_I} (\sin(2\pi ft + \theta) + 1) dt \right]}{n!}, \quad (13)$$

where $j = 1, 2, \dots, j_{\max}$, and $\sin(2\pi f_M t + \theta) + 1$ is the modulation function. According to Eq. (13), the formula of Mandel- Q parameter changes to

$$Q = \frac{\langle n^2 \rangle_M - \langle n \rangle_M^2}{\langle n \rangle_M} - 1, \quad (14)$$

where

$$\langle n^2 \rangle_M = \frac{\sum_{j=0}^{j_{\max}} \sum_{n=0}^{\infty} P_n^M \cdot n^2}{j_{\max}}, \quad (15)$$

$$\langle n \rangle_M = \frac{\sum_{j=0}^{j_{\max}} \sum_{n=0}^{\infty} P_n^M \cdot n}{j_{\max}}. \quad (16)$$

As shown in Fig. 7(b), with the increase of integration time Mandel- Q parameter oscillates periodically. When $T_i \gg 1/f_M$, that is, the integration time is much bigger than the modulation period, the average effect will eliminate the influence of the modulation.

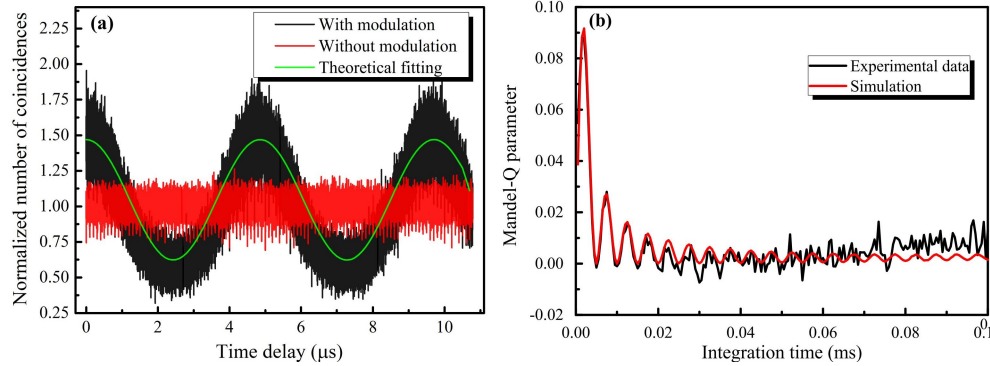


Fig. 7. Experimental result of the second-order correlation function and Mandel- Q parameter measurement. In (a), the black and red line indicates the second-order correlation function of a single-photon sequence with and without modulation. The green line is the theoretical fitting using Eq. (9). In (b), the black and red line are experimental and simulation results, respectively; the mismatch of the experimental result and the simulation result is caused by the limited sampling time. The experimental data were acquired with the help of a time interval analyzer (GT658).

Appendix B: algorithm flowchart of the simulation

We used the Monte Carlo method for the simulation, Fig. 8 is the algorithm flowchart. First, a set of random number $t'_i \in (0, T_i]$ is generated to simulate the random arrival time of the photons of the coherent state. In the experiment, the emission probability of a photon increases in proportion to the amplitude of modulation signal $s_i = \sin(2\pi f_M t'_i) + 1$; therefore, in the simulation, another random number A_i , which uniformly distribute in the $(0, 2]$, is generated. The probability that A_i is bigger than s_i is the same as the emission probability of the photon. The time jitter and the noisy counts are easy to add in the simulation as shown in the algorithm flowchart. We assume the noisy count, including the background and dark count, obeys Poisson distribution. Finally, the DFT is implemented to the arrival time $t = t_1, \dots, t_1, \dots, t_{c+n}$ (c and n are the signal photon counts and noise count within one integration time) to calculate the amplitude of the characteristic spectral line A_S and the amplitude of the noise floor A_B . By running the program multiple times, the distribution of the A_S and A_B can be obtained, so does their mean value and variance.

Appendix C: transmission capacity

Assume the input variable of a noisy channel is X , and the output is Y . According to the Noisy-channel coding theorem, the channel capacity is $C=I(X;Y)$, where $I(X;Y)=H(Y)-H(Y|X)$ is the mutual information and $H(x)=-x\text{Log}(x)-(1-x)\text{Log}(1-x)$ is the binary entropy function. $H(Y)$ is the marginal entropy and $H(X|Y)$ is the conditional entropy. For the binary symmetric channel, $H(Y)=1$ when the input has equal probability to be 0 or 1. The conditional entropy $H(X|Y)$ could be expressed as

$$H(Y|X) = -\sum_{x \in X} p(x) \sum_{y \in Y} p(y|x) \text{Log} p(y|x). \quad (17)$$

For binary symmetric channel

$$H(Y|X) = H(p_e) = -p_e \text{Log} p_e - (1-p_e) \text{Log} (1-p_e), \quad (18)$$

where p_e is the bit error rate. According to the above analysis, the channel capacity is $C = H(Y)-H(Y|X) = 1-H(p_e)$, here, C could be explained as the average amount of information that receiver can get from each bit when considering the bit error rate. The transmission capacity in this paper means the maximal transmission rate per second. The maximal number of combinations of modulation frequencies is M_{max} which means $\text{Log}_2 M_{max}$ bits will be transmitted within one integration time T_i ; therefore, the bit rate per second would be $(1/T_i)*\text{Log}_2 M_{max}$. According to the above analysis, the final transmission capacity could be expressed by Eq. (7). For a binary system, the bit error rate p_e could be simply calculated from

$$p_e = \frac{\text{Number of error bits}}{\text{Total transmitted bits}}. \quad (19)$$

But for the multi-state systems, the bit error rate p_e is not equal to the error rate e . For instance, in our system, the maximal degree of freedom is M_{max} , which means we can transmit $k=\text{Log}_2 M_{max}$ bits of information in one-time transmission. Assume that each bit has the same probability to be 0 or 1; therefore, when we failed to decode the modulation frequency correctly, there are half chance for each bit to be an error. Therefore, the bit error rate is

$$p_e = \frac{2^{k-1}}{2^k - 1} e, \quad (20)$$

and because $M_{max} = 2^k$, the bit error rate could also be expressed as $p_e = M_{max}e/2(M_{max}-1)$.

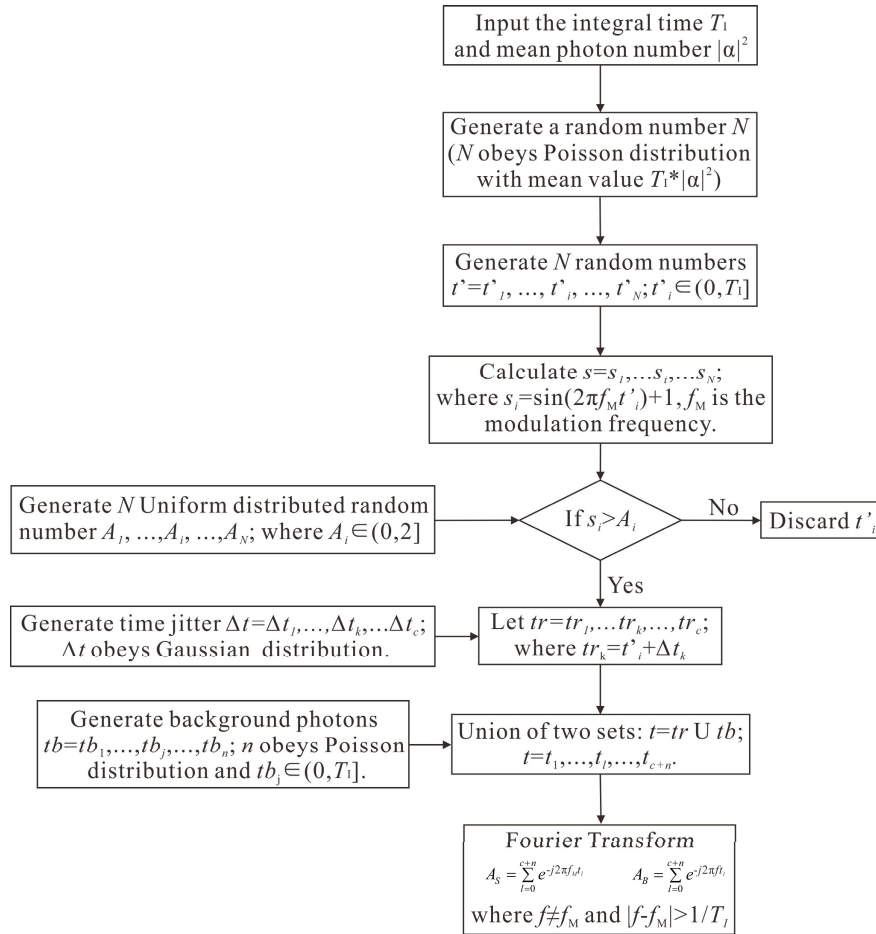


Fig. 8. Algorithm flowchart of the simulation.

Funding

The National Key R&D Program of China (2017YFA0304203); Natural Science Foundation of China (61527824, 61675119); PCSIRT (IRT 13076).

Acknowledgments

We thank the high-performance simulation platform of Shanxi University for providing computing resources.

References

1. G. Vallone, D. Bacco, D. Dequal, S. Gaiarin, V. Luceri, G. Bianco, and P. Villoresi, "Experimental Satellite Quantum Communications," *Phys. Rev. Lett.* **115**(4), 040502 (2015).
2. Q. Wang, L. Tong, S. Yu, L. Tan, and J. Ma, "Accurate beacon positioning method for satellite-to-ground optical communication," *Opt. Express* **25**(25), 30996–31005 (2017).
3. J. Yin, Y. Cao, S. B. Liu, G. S. Pan, J. H. Wang, T. Yang, Z. P. Zhang, F. M. Yang, Y. A. Chen, C. Z. Peng, and J. W. Pan, "Experimental quasi-single-photon transmission from satellite to earth," *Opt. Express* **21**(17), 20032–20040 (2013).
4. S. K. Liao, H. L. Yong, C. Liu, G. L. Shentu, D. D. Li, J. Lin, H. Dai, S. Q. Zhao, B. Li, J. Y. Guan, W. Chen, Y. H. Gong, Y. Li, Z. H. Lin, G. S. Pan, J. S. Pelc, M. M. Fejer, W. Z. Zhang, W. Y. Liu, J. Yin, J. G. Ren, X. B. Wang, Q. Zhang, C. Z. Peng, and J. W. Pan, "Long-distance free-space quantum key distribution in daylight towards inter-satellite communication," *Nat. Photonics* **11**(8), 509–513 (2017).
5. X. Sun, D. R. Skillman, E. D. Hoffman, D. Mao, J. F. McGarry, L. McIntire, R. S. Zellar, F. M. Davidson, W. H. Fong, M. A. Krainak, G. A. Neumann, M. T. Zuber, and D. E. Smith, "Free space laser communication

- experiments from Earth to the Lunar Reconnaissance Orbiter in lunar orbit,” *Opt. Express* **21**(2), 1865–1871 (2013).
6. A. A. Kazemi, “Intersatellite Laser Communication System for Harsh Environment of space,” *Proc. SPIE* **8720**, 872010 (2013).
 7. M. L. Stevens, D. O. Caplan, B. S. Robinson, D. M. Boroson, and A. L. Kachelmyer, “Optical homodyne PSK demonstration of 1.5 photons per bit at 156 Mbps with rate-1/2 turbo coding,” *Opt. Express* **16**(14), 10412–10420 (2008).
 8. M. R. Abaza, N. A. Mohammed, and M. H. Aly, “BER performance of M-ary PPM freespace optical communications with channel fading,” in *Proceedings of international conference on high capacity optical networks and enabling technologies*, Riyadh, Saudi Arabia, (2011), pp. 111–115.
 9. G. Contestabile, P. Velha, and N. Andriolli, “High-Speed InP-Integrated Pre-Amplified Demodulator for WDM-DPSK Signals,” *IEEE Photonic Tech. Lett.* **27**(24), 2547–2550 (2015).
 10. N. Krstajić, S. Poland, J. Levitt, R. Walker, A. Erdogan, S. Ameer-Beg, and R. K. Henderson, “0.5 billion events per second time correlated single photon counting using CMOS SPAD arrays,” *Opt. Lett.* **40**(18), 4305–4308 (2015).
 11. C. Guerlin, J. Bernu, S. Deléglise, C. Sayrin, S. Gleyzes, S. Kuhr, M. Brune, J. M. Raimond, and S. Haroche, “Progressive field-state collapse and quantum non-demolition photon counting,” *Nature* **448**(7156), 889–893 (2007).
 12. N. Demoli, H. Skenderović, and M. Stipčević, “Time-averaged photon-counting digital holography,” *Opt. Lett.* **40**(18), 4245–4248 (2015).
 13. D. Braun and A. Libchaber, “Computer-based photon-counting lock-in for phase detection at the shot-noise limit,” *Opt. Lett.* **27**(16), 1418–1420 (2002).
 14. Z. Zhang, Y. Xu, L. Wu, Y. Zhang, Y. Zhao, and J. Su, “Photon counting range-intensity image strategy in low-light level environments,” *Opt. Lett.* **39**(8), 2467–2470 (2014).
 15. X. B. Wang, J. J. Wang, G. F. Zhang, L. T. Xiao, and S. T. Jia, “Photon counts modulation in optical time domain reflectometry,” *Chin. Phys. B* **20**(6), 064204 (2011).
 16. M. A. Albota and B. S. Robinson, “Photon-counting 1.55 μm optical communications with pulse-position modulation and a multimode upconversion single-photon receiver,” *Opt. Lett.* **35**(15), 2627–2629 (2010).
 17. T. Iwata, A. Hori, and T. Kamada, “Photon-Counting Phase-Modulation Fluorometer,” *Opt. Rev.* **8**(5), 326–330 (2001).
 18. H. A. M. Leymann, A. Foerster, F. Jahnke, J. Wiersig, and C. Gies, “Sub- and Superradiance in Nanolasers,” *Phys. Rev. Appl.* **4**(4), 044018 (2015).
 19. R. Alléaume, F. Treussart, J. M. Courty, and J. F. Roch, “Photon statistics characterization of a single-photon source,” *New J. Phys.* **6**(1), 85 (2004).
 20. S. Meuret, L. H. Tizei, T. Cazimajou, R. Bourrellier, H. C. Chang, F. Treussart, and M. Kociak, “Photon Bunching in Cathodoluminescence,” *Phys. Rev. Lett.* **114**(19), 197401 (2015).
 21. F. Treussart, R. Alléaume, V. Le Floch, L. T. Xiao, J. M. Courty, and J. F. Roch, “Direct Measurement of the Photon Statistics of a Triggered Single Photon Source,” *Phys. Rev. Lett.* **89**(9), 093601 (2002).
 22. Y. Liu, B. Yu, B. He, G. F. Zhang, L. T. Xiao, and S. T. Jia, “Single-photon modulation spectrum,” *Chin. Phys. B* **23**(1), 010101 (2014).
 23. J. Y. Hu, Y. Liu, L. L. Liu, B. Yu, G. F. Zhang, L. T. Xiao, and S. T. Jia, “Quantum description and measurement for single photon modulation,” *Photon. Res.* **3**(1), 24–27 (2015).
 24. M. Ren, E. Wu, Y. Liang, Y. Jian, G. Wu, and H. P. Zeng, “Quantum random-number generator based on a photon-number-resolving detector,” *Phys. Rev. A* **83**(2), 023820 (2011).
 25. J. S. Lundeen, B. Sutherland, A. Patel, C. Stewart, and C. Bamber, “Direct measurement of the quantum wavefunction,” *Nature* **474**(7350), 188–191 (2011).
 26. J. Wiersig, C. Gies, F. Jahnke, M. Assmann, T. Berstermann, M. Bayer, C. Kistner, S. Reitzenstein, C. Schneider, S. Höfling, A. Forchel, C. Kruse, J. Kalden, and D. Hommel, “Direct observation of correlations between individual photon emission events of a microcavity laser,” *Nature* **460**(7252), 245–249 (2009).
 27. N. Ramírez-Cruz, M. A. Bastarrachea-Magnani, and V. Velázquez, “Quantum Anatomy of the Classical Interference of n -Photon States in a Mach-Zehnder Interferometer,” *J. Phys. Conf. Ser.* **698**(1), 012015 (2016).
 28. Y. Dwivedi and S. Subba Rao, “A test for second-order stationarity of a time series based on the discrete Fourier transform,” *J. Time Ser. Anal.* **32**(1), 68–91 (2011).
 29. J. Y. Hu, B. Yu, M. Y. Jing, L. T. Xiao, S. T. Jia, G. Q. Qin, and G. L. Long, “Experimental quantum secure direct communication with single photons,” *Light Sci. Appl.* **5**(9), e16144 (2016).
 30. S. A. Abbas, Q. Sun, and H. Foroosh, “Frequency estimation of sinusoids from nonuniform samples,” *Signal Process.* **129**, 67–81 (2016).
 31. J. C. Hoch, M. W. Maciejewski, M. Mobli, A. D. Schuyler, and A. S. Stern, “Nonuniform Sampling and Maximum Entropy Reconstruction in Multidimensional NMR,” *Acc. Chem. Res.* **47**(2), 708–717 (2014).
 32. M. Mobli and J. C. Hoch, “Nonuniform sampling and non-Fourier signal processing methods in multidimensional NMR,” *Prog. Nucl. Magn. Reson. Spectrosc.* **83**, 21–41 (2014).